Ice in convective storm environments: assessing impacts of microphysics on simulated reflectivities

Julia A. Shates[a], Derek J. Posselt[a], Matthew D. Lebsock[a], Joseph A. Finlon[b c], Greg M. McFarquhar[d e], Andrew J. Heymsfield[f]

[a] *Jet Propulsion Laboratory, California Institute of Technology, Pasadena, CA,* [b] *NASA Goddard Space Flight Center, Greenbelt, Maryland,* [c] *Earth System Science Interdisciplinary Center, University of Maryland, College Park, College Park, Maryland,* [d] *Cooperative Institute for Severe and High Impact Weather Research and Operations, University of Oklahoma, Norman, OK,* [e] *School of Meteorology, University of Oklahoma, Norman, OK, USA* [f] *NSF National Center for Atmospheric Research, Boulder, CO, United States of America*

Corresponding author: Julia A. Shates, julia.shates@gmail.com

ABSTRACT: Satellite radar retrievals of clouds and precipitation rely on assumptions about the microphysical properties of hydrometeors such as particle size distributions (PSDs) and mass-dimensional relationships, which have been shown to vary in distinct environments. A deeper understanding of linkages between mass-dimensional relationships, ice crystal shape, and radar reflectivities across cloud and precipitation regimes is necessary for developing new retrievals for upcoming satellite radar missions, including the INvestigation of Convective UpdraftS (INCUS), as well as future missions that will feature space-borne radars observing clouds, convection, and precipitation. This study investigates ice microphysical characteristics through aircraft in-situ and remote sensing observations from two convective events during the Mid-latitude Continental Convective Clouds Experiment (MC3E) in the Southern Great Plains, and tests implications for ice particle habit in forward modeled radar observations. During MC3E, the Ka/Ku- band High Altitude Imaging Wind and Rain Airborne Profiler (HIWRAP) was onboard the NASA ER-2 aircraft, while in-situ measurements were taken onboard the University of North Dakota Citation. In-situ PSDs and particle shape information from optical array probe data are used to forward model radar reflectivities from particle scattering databases and are compared against HIWRAP reflectivities. Various particle combinations can be used to find agreement with HIWRAP observations, and the forward modeled reflectivities were sensitive to particle type. Varying the riming on the aggregate and graupel particles resulted in larger than 10 dB differences in reflectivities. The in-situ and radar observations imply the occurrence of aggregation, size sorting and lofting particles.

SIGNIFICANCE STATEMENT: Ice particles in the atmosphere are diverse in shape and number concentration, and vary in different cloud and precipitation environments. It is important to understand how variations in their mass, shape, and number may influence remote sensing observations to develop deeper understanding for future satellite radar retrievals. This work uses field campaign observations of ice particles measured by in-situ probes onboard aircraft combined with radar onboard a second aircraft. The in-situ measurements are used to simulate radar observations, and the simulations are compared to the aircraft radar observations. The results show the particle mixtures can be used to obtain realistic simulated signals, but the assumptions on particle characteristics influence the results.

1. Introduction

Ice microphysical characteristics influence weather and climate via their effects on radiative transfer, precipitation, and latent heating. Most stratiform rainfall in the mid-latitudes results from melting snowflakes (Field and Heymsfield 2015; Schumacher and Funk 2023), and ice microphysical processes aloft influence the rain at the surface (Kumjian et al. 2016; Prein and Heymsfield 2020; Li et al. 2022, 2024). Anvil clouds formed from thunderstorm outflows have radiative impacts (Stephens et al. 2024) on large climate scales. Aircraft field campaign studies have shown that ice microphysical characteristics such as particle size distributions (PSDs) and crystal shapes differ in distinct cloud types and environments such as cirrus that form in-situ vs. anvil cirrus (Heymsfield et al. 2013a; Lawson et al. 2019; Krämer et al. 2020) and stratiform clouds (Liu et al. 2022). Ice particles grow and form into distinct habits as a result of their environment (temperature and ice supersaturation) (Nakaya 1954; Libbrecht 2017; Hueholt et al. 2022). Ground-based observations have been used to show how variability in precipitation microphysics at the surface relates to the environment and different kinds of regimes (i.e stratiform/convective) in rainfall (Dolan et al. 2018) and snowfall (King et al. 2024). DeLaFrance et al. (2024) investigate ice phase particle evolution with aircraft observations and habit information to assess impact of microphysical processes such as riming in orographic snowfall. Exploring the variability of microphysics in ice clouds for different types of clouds and storm events is valuable for developing a priori information for satellite radar retrievals (Liu and Illingworth 2000; Delanoë and Hogan 2008).

In order to develop retrievals of cloud/precipitation properties from remote sensing observations, it is necessary to have a relationship between particle mass and size and backscatter cross-section to then connect to reflectivity observations. Locatelli and Hobbs (1974) related size, mass and fall speed for solid precipitation particles with various particle types from dendrites to columns to various kinds of graupel. The empirical relationships found in this study continue to be the basis for current day understanding of mass-dimensional (m-D) relationships. Brown and Francis (1995) and Heymsfield et al. (2010), referred to BF95 and HY10 respectively, used aircraft optical array probes and ice water content measurements during field campaigns to derive the mass-dimensional relationships. While these m-D relationships have been widely used, studies have shown that there are a range of plausible m-D relationships that agree with the available observations (Finlon et al. 2019). Different methods have been developed to improve and expand upon previous m-D relationships.. Mascio et al. (2017) explored m-D relationships in tropical anvil cirrus clouds using optimal estimation algorithms. Multiple studies have highlighted utility in using multiple radar frequencies (e.g. Dual Frequency Ratios [DFRs]) with in-situ observations (Kneifel et al. 2011; Tridon et al. 2019; Chase et al. 2021; Duffy et al. 2021; Finlon et al. 2022; Heymsfield et al. 2023; Sy et al. 2020). The DFR does not depend on the number concentration and provides information specifically relevant to the size of the particles. Other radar observations provide additional context for constraining mass-dimensional relationships such as Doppler (Maahn et al. 2015) and dual polarization capabilities (Mace et al. 2023).

Forward modeling, defined here as algorithms used to simulate remote sensing measurements from geophysical variables, is used to evaluate the effect of changes in ice crystal properties on radar measurements. Forward models are used in retrievals (Maahn et al. 2020), data assimilation (Janisková and Fielding 2020), and model evaluation (Kay et al. 2012; Hutson et al. 2025). Radar forward models have been developed for satellite radars (EarthCARE; Roh et al., 2023; Kollias et al., 2023) and ground-based radar (Cloud-resolving model Radar SIMulator [CR-SIM]; Oue et al., 2020). It is important to emphasize that in these forward models, decisions must be made in how to represent liquid and ice particles and their scattering properties (Sy et al. 2020; Oue et al. 2020).

This study seeks to relate in-situ and remote sensing aircraft measurements by forward modeling observations from a field campaign focused on ice clouds/precipitation associated with deep convection. Ice microphysical characteristics associated with convection are of particular interest for the INvestigation of Convective UpdraftS (INCUS; van den Heever, 2021; Dolan et al., 2023) satellite mission, which will estimate convective vertical mass flux from changes in Ka-band reflectivities in deep convection. In addition, INCUS will estimate the ice content in convective anvils. This study uses observations from the aircraft in the Mid-latitude Continental Convective Clouds Experiment (MC3E; Jensen et al., 2016), which sampled ice particles in multiple convective storms with in-situ probe measurements of cloud properties, as well as radar remote sensing observations at Ku- and Ka-band frequencies. The methods used for exploring the microphysics and radar observations of continental convection from the MC3E can be applied to field campaigns with similar aircraft and instrumentation to further assess ice properties in other regions. In this study, we use MC3E observations along with a forward model that accommodates a range of ice cloud properties to:

1. examine ice microphysical properties (PSDs, habits) observed in the stratiform region following a convective line and in anvil outflow from supercell convection,

2. explore the impact of varying riming in habit mixtures on forward modeled reflectivities, and compare to radar observations

3. assess the implications of assumptions on the types of particles used in forward modeling, and guide further efforts to use observations to constrain the range of possible ice microphysical characteristics in retrievals.

2. Data and Methods

a. Mid-latitude Continental Convective Clouds Experiment

MC3E included ground-based and air-borne observations of spring-time convective events with flights in April, May and June of 2011. MC3E was part of a greater effort coordinated under the Global Precipitation Measurement (GPM) mission to produce datasets suited for assessing and characterizing satellite radar observations (Jensen et al. 2016; Heymsfield et al. 2013b). The work here is focused on two well-documented events during MC3E. The first event was a convective line followed by extensive trailing stratiform shield precipitation on 20 May 2011. The second event featured a convective supercell on 23 May 2011. In this work, the cases are referenced as the convective line stratiform shield (20 May) and supercell anvil outflow (23 May) to highlight the convective environment and the regimes that were sampled. These two cases provide a unique dataset to explore microphysics and radar remote sensing between collocated aircraft measurements. Different aspects of these events have been investigated: the microphysics and conditions associated with a sagging brightband in stratiform rainfall from the ground-based radar observations (Kumjian et al. 2016); regional modeling studies of microphysics impacting mesoscale convective systems (MCSs) (Marinescu et al. 2016); aircraft radar observations and vertical motions during hailstorms Heymsfield et al. (2013b); and microphysical characteristics of ice clouds (Finlon et al. 2019; Duffy et al. 2021; Duffy and Posselt 2022; Dzambo et al. 2023).

b. In-situ observations

The University of North Dakota Citation aircraft was used to fly in-situ probes through clouds and precipitation in MC3E. Several instruments hosted on the Citation measured cloud environmental conditions, including temperature, water vapor mixing ratio, air pressure, and vertical velocity. Of the in-situ cloud probe measurements available, we analyze observations from the 2D - Cloud Imaging Probe (2DC) and the High-Volume Precipitation Spectrometer (HVPS). The 2DC and HVPS obtain images of ice and liquid particles. The 2DC is used to characterize particles between 150 μm and 1 mm.The HVPS size bins range cover the range 0.25 to 19.2 mm. There is an overlap in sizes observed between the 2DC and the HVPS - in order to not overcount particles, the 2DC is used for sizes less than 1 mm, and the HVPS observations are used for sizes greater than 1 mm. The particle bin width (resolution) also varies with particle size as larger bin widths are needed to maintain sufficient sampling statistics of larger particles. For small particles with dimensions less than 5 mm, the bin width is 0.05 mm, and the bin width increases to 1 mm at particle sizes ranging 5-10 mm.

The 2DC and HVPS data are processed using the University of Illinois/Oklahoma Optical Array Probe (OAP) Processing Software (UIOOPS_v3.4; McFarquhar et al., 2018) to obtain particle size and shape distributions. The habit identification algorithm in UIOOPS is based on the methodology described in Holroyd III (1987), which evaluates image structure and size in a decision tree format. The method was originally developed for the 2DC, but processing has been updated for the larger particle sizes measured by the HVPS. In any automated identification method, there are inherent uncertainties in the results. Schima et al. (2024) assess the UIOOPS on OAPs; one of the challenges in detecting some habits such as plates and dendrites is from the particle sizes and probe resolution. Variables output from UIOOPS include the particle maximum dimension (D), number concentration (N_t) and the particle size distribution (PSD), among other bin and bulk properties for particles with D > 150 μm. By only using particles with D > 150 μm, uncertainties in observing smaller particles are avoided (e.g. uncertainties caused by a small depth of field for the OAP and the potential impact of shattering on probe tips). 10-second discrete averaging is applied to both the PSDs and N_t measurements. The particles are sorted into seven habit categories: Spherical, Linear, Hexagonal, Irregular, Graupel, Dendrite, and Aggregate. An eighth category, referred to as "Tiny", is reserved for particles that are too small to be classified because of pixel resolution (D≤ .3 mm for the 2DC and D≤ 1 mm for the HVPS) (Schima et al. 2024). In this study, the tiny particles are merged into the irregular category.

c. Remote Sensing Observations

The High Altitude Imaging Wind and Rain Airborne Profiler (HIWRAP; Heymsfield et al., 2013b; Li et al., 2015) was installed on the NASA ER-2 during MC3E. The HIWRAP is a dual frequency Doppler radar observing clouds and precipitation at the Ka/Ku–bands (35 GHz/13 GHz) with a range resolution of 75 m. The HIWRAP was sampling clouds and precipitation at nadir pointing configuration during MC3E with the goal fo emulating the Ka/Ku-band radar of the GPM Dual-frequency Precipitation Radar. The minimum detectable reflectivities for the Ka/Ku-bands are -5dBZ and -10 dBZ (Heymsfield et al. 2013b). Attenuation corrections were not applied to the radar observations. An offset is used to calibrate the Ka-band reflectivties. In Rayleigh regimes, the difference between the Ku- and Ka-band reflectivities should be zero (Tanelli et al. 2006), and in order to maintain this, an offset is used to match them (Heymsfield et al. 2013b; Chase et al. 2021; Duffy et al. 2021). The offsets are variable across field campaigns and different events (Duffy et al. 2021). In Heymsfield et al. (2013b) the HIWRAP Ka-band reflectivites for two MC3E flights (23-24 May 2011) were adjusted downward to match the Ku-band by~ 1.7 dB. In this work, the Ka-band reflectivities are adjusted downward by 0.5 - 0.75 dB on 23 May (supercell anvil outflow) and 1 dB on 20 May (stratiform shield).

Data from the operational weather radar (Next Generation Weather Radar; NEXRAD; S-band /10 cm wavelength) located at Vance Airforce Base, Oklahoma (identifier KVNX) are used to provide context for the airborne observations. These NEXRAD data have previously been analyzed alongside in-situ probe data for the MC3E in studies assessing microphysics and reflectivities (Finlon et al. 2019; Dzambo et al. 2023). In addition to ancillary ground-based observations, spaceborne observations of brightness temperatures from GOES-13 (Channel 3, IR water vapor, ~6.7 microns) (Knapp and Wilkins 2018) also provide information on storm extent and evolution.

d. Collocating Aircraft Observations

There are numerous methods for collocating observations between multiple aircraft platforms. In the following analysis, observations from the ER-2 and Citation were collocated using spatial and temporal criteria based on thresholds defined by Chase et al. (2018): within 1 km in horizontal distance and within 10 minutes observation time. First, 1 km is used as the upper threshold for the distance between the ER-2 and Citation aircraft flight paths. Then, the distinct flight legs are temporally collocated with an upper limit of 10 minutes. Some collocation methods construct radar observations time series that are directly matched to the in-situ data (e.g., Finlon et al., 2022; Tridon et al., 2019). Because the two aircraft rarely flew in formation during MC3E, we use an approach that permits some flexibility in the collocation requirements. Following collocation, distributions of observed and simulated reflectivities are compared for the distinct flight legs at each height level. The mean heights of the Citation during the collocated leg are used to obtain radar range gates from the HIWRAP.

Figures 1 and 2 show examples of two collocated legs for the convective line shield stratiform (20 May) and the supercell anvil outflow (23 May), respectively. The GOES-13 brightness temperatures show the large-scale extent of the clouds, and the NEXRAD PPI shows radar reflectivities at the lowest angle scan associated with each event. The flight paths of the ER-2 and Citation within the 10-minute threshold are plotted on the maps. Multiple PPIs at all angle scans are compiled to create a cross section along an azimuth intersecting the flight paths. In Figure 1, the GOES-13 data shows the convective line, with the trailing stratiform structure exhibiting higher brightness temperatures than east along the line. The NEXRAD PPI lowest angle scan shows widespread precipitation, while the cross section through the stratiform region shows the reflectivities increase downwards towards the melting level (~4 km ASL) where the reflectivities increase downwards towards the melting level. In Figure 2, cold anvils extend beyond the convective supercells. The lowest angle scan of the NEXRAD depicts distinct cells with high reflectivities, while the GOES13 brightness temperatures show cold anvil clouds connecting distinct convective cells and nearly filling the NEXRAD domain. The flight paths overlaid on the GOES13 and NEXRAD PPI plots are slightly offset in time from each other (~3 minutes), and show the aircraft repetitively sampled the same anvil outflow region. The NEXRAD cross section shows that the anvil clouds, defined as reflectivities greater than 5 dBZ, extended above 8 km AGL.

e. Forward Modeling

The forward model used in this study produces radar reflectivities at Ka- and Ku-band wavelengths from in-situ measurements of discrete PSDs for each of the seven habit categories defined earlier. Generally, radar simulators require the hydrometeor type to be predefined to represent its mass-dimensional and scattering properties, and various databases have been developed for this purpose. Each category is matched to a named particle type from existing particle scattering databases. Two databases are utilized in this study. The Atmospheric Radiative Transfer Simulator (ARTS) Microwave Single Scattering Properties Database (Eriksson et al. 2018; Buehler et al. 2018) uses the discrete dipole approximation (DDA) to calculate scattering for individual particles. The snowScatt database (Ori et al. 2021) contains particle scattering properties from the Self Similar Rayleigh-Gans Approximation (SSRGA; Hogan and Westbrook, 2014) for ensembles of particles with varying degrees of rime (Maherndl et al. 2023; Leinonen and Szyrmer 2015). The rimed aggregates in snowScatt are based on Leinonen and Szyrmer (2015), which describe that the amount of rime is defined according to the effective liquid water path (ELWP) through which the particle is assumed to have fallen. The ELWP assumes the particles have a riming efficiency equal to 1; i.e., every collision between an ice particle and a liquid droplet is assumed to result in collection of the liquid droplet by the ice particle. This assumption is used to ensure that the riming results in consistent and correct quantities of mass on the snowflakes. Table 1 documents how the particle types are matched between the UIOOPS categories and the ARTS and snowScatt particles. The ARTS and snowScatt databases include particle characteristics that can be used to simulate reflectivities for multiple frequencies. Each particle habit has a prescribed m-D relationship and

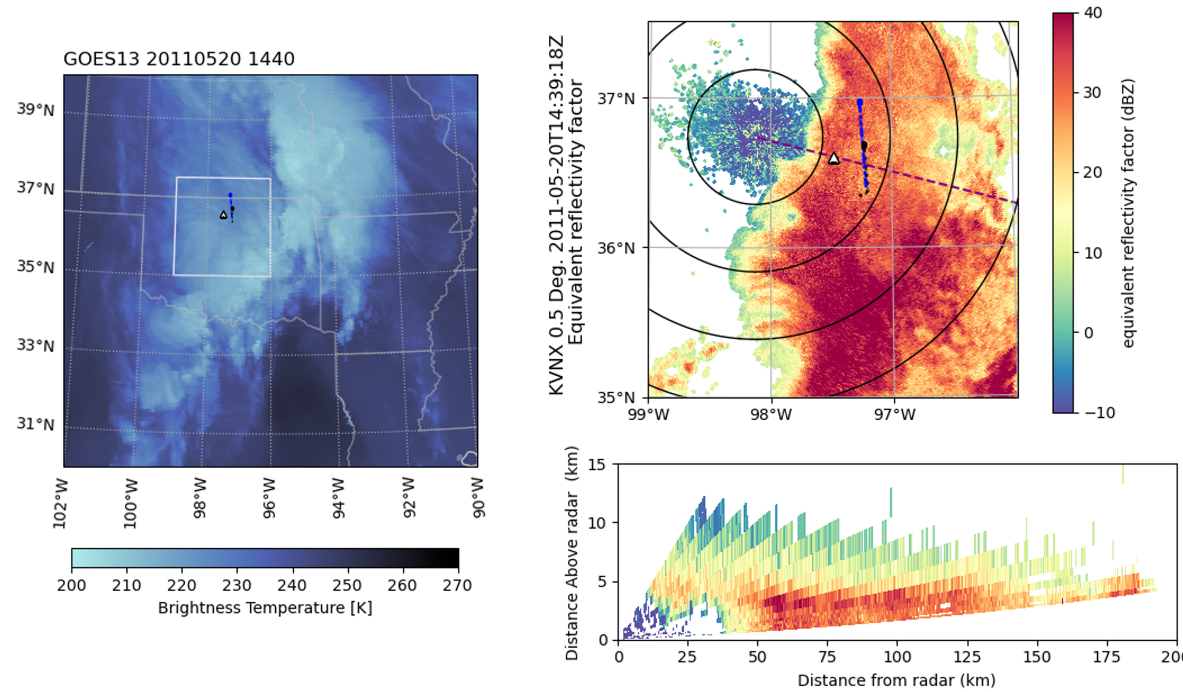

FIG. 1. GOES-13 and NEXRAD observations from KVNX for 20 May 2011. The left plot (a) shows GOES-13 brightness temperatures at 1440 UTC, and the right plots show NEXRAD PPI (b) and cross section (c) for 1439 UTC. The purple dashed line on the PPI shows the azimuth line for the cross section. The ER-2 and Citation flight paths during the 5 minutes leading up to the PPI scan and GOES-13 snapshot are shown in blue dashed and black dotted lines, respectively. The range rings on the PPI scans are 50 km intervals. Note: the altitude of the radar is 378 meters ASL. For additional context, the ARM SGP site is shown with a triangle symbol on a and b. NEXRAD PPI scans and PPI to cross sections were plotted using the Python ARM Radar Toolkit (Py-ART; Helmus and Collis, 2016).

scattering properties. This study uses aggregates that are formed with simultaneous aggregation and riming (”A” scenario from Leinonen and Szyrmer, 2015). Aggregates with various degrees of riming/ELWP are included from the SnowScatt database; in this study, the ELWP ranges from 0.0 kg m^{-2} (no riming) to 1.0 kg m^{-2}. We test two distinct assumptions for graupel: a lightly rimed Leinonen aggregate (Leinonen15 A01) and a fully rimed Leinonen graupel particle (Leinonen15 C). Figure 3 shows the m-D relationships for the particle habits shown in Table 1. The particle mass for a given size can vary substantially depending on the different habits. The m-D relationships

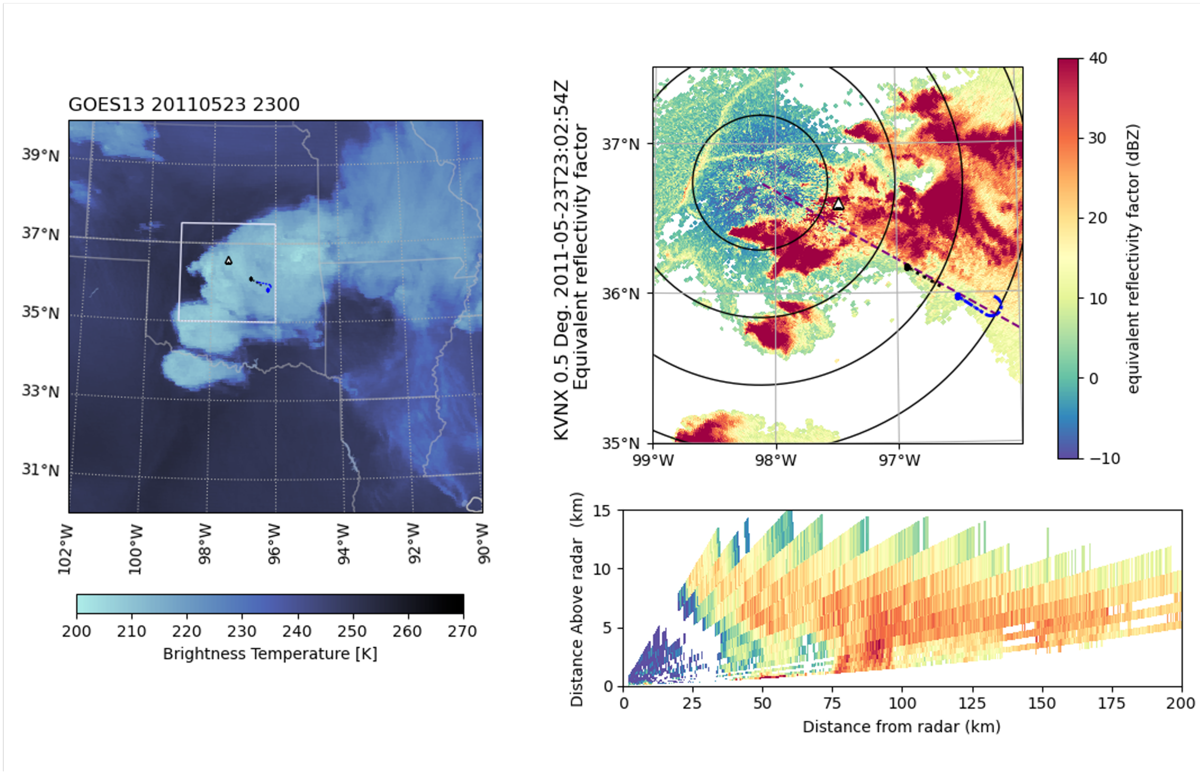

FIG. 2. Same as in Fig. 1 but for 23 May 2011 ~23 UTC.

TABLE 1. Ice particle habits used for habit mixtures ("HX" in figure legends) forward modeling with in-situ

UIOOPS	database	particles	description
Spherical	ARTS	IconCloudIce	spheroidal, low aspect ratio
Linear	snowScatt	vonTerzi_mixcoldend	assemblages of mixtures of columns and dendrites
Hexagonal	ARTS	PlateType1	hexagonal plate
Irregular	ARTS	SmallPlateAggregate	hexagonal plate aggregates
Graupel	snowScatt	Leinonen15 A01 Leinonen15 C	lightly rimed snowflake rime only graupel
Dendrite	snowScatt	Leinonen1500	unrimed snowflake
Aggregate	snowScatt	Leinonen15 A00 Leinonen15 A01 Leinonen15 A02 Leinonen15 A05 Leinonen15 A10	snowflakes with increasing ELWP for riming

estimated by HY10 and BF95 are also shown for reference. The BF95 m-D relationship was developed with observations from mid-latitude cirrus clouds, while the HY10 m-D relationship includes observations from several field campaigns from synoptic to convective ice clouds (anvils) in various regions.

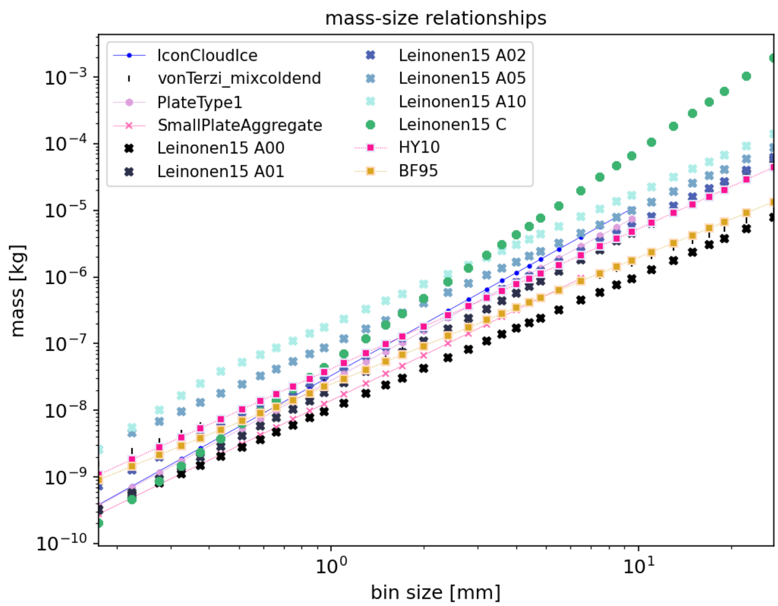

FIG. 3. Mass-size curves for database particles. The figure shows select particle habits and their mass-dimensional relationships from ARTS and snowScatt. The ARTS particles are indicated by having a solid line on the plots, whereas snowScatt particles have markers without a solid line.

3. Results

We first describe the microphysical characteristics and the environmental (temperature) conditions of the in-situ observations, and then discuss the remote sensing observations and forward modeling data. Detailed examples from the convective line stratiform shield (20 May) and anvil outflow (23 May) can be found in the remote sensing section, and include PSDs, HIWRAP reflectivities and distributions of forward modeled reflectivities. Following the detailed examples, the subsection summarizes the reflectivities and DFRs for multiple collocated legs.

a. Microphysics and Environment

The two MC3E events sampled different regimes of ice particles at different altitudes and temperatures within the stratiform shield following a convective line (20 May) and within supercell anvil outflow (23 May). Figure 4a,b show the altitudes and temperatures where ice particles were observed by the OAPs and collocated with the ER-2. The temperatures in the stratiform shield

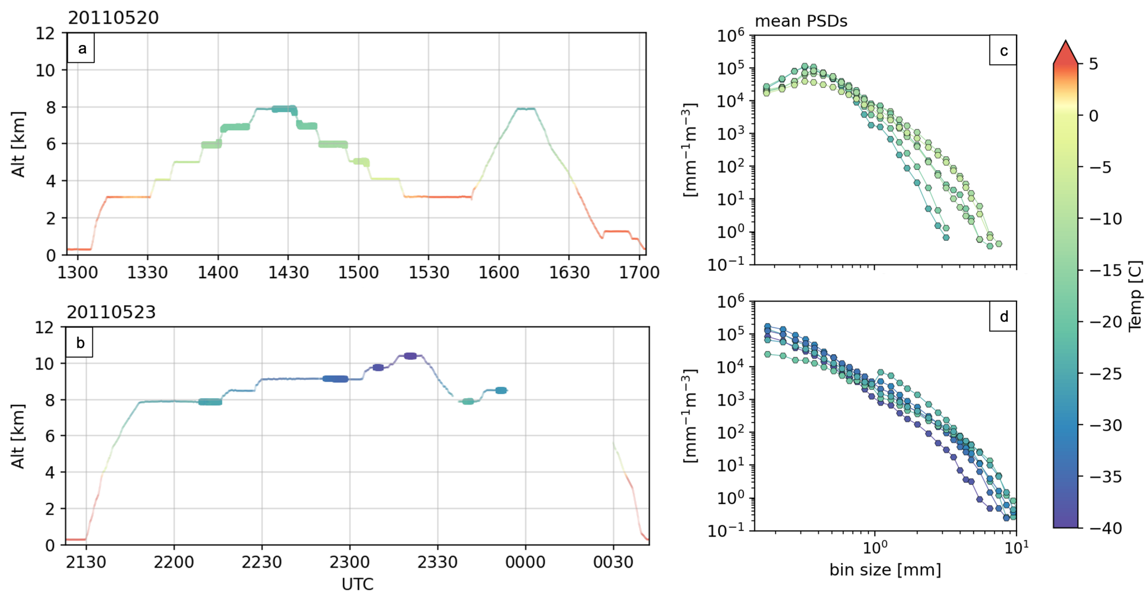

FIG. 4. Altitude, temperature, and in-situ mean PSD (a,c) 20 May 2011 and (b,d) 23 May 2011. The light-gray dotted line shows the altitude of the Citation for the entire observational period (a,b). Lines marked with temperature data show where both ice clouds are observed by the OAPs and indicate a spatial collocation with the ER-2. On (c) and (d), the mean PSD is shown for the corresponding altitudes and legs. The marker colors for the mean PSDs show the mean temperature of the Citation leg/section. The warmest temperature included above is -0.8° C, which was observed 20 May 2011. The coldest temperature included above is -42° C from 23 May 2011.

from 4 to 8 km ASL range from 0° C to -23° C. In the supercell anvil outflow, OAPs observed ice particles from 8 km ASL to ~10 km ASL where temperatures ranged from -20° C to -43° C.

Figure 4c,d shows the corresponding mean PSDs for each of the legs shown in Fig. 4a,b. The mean PSDs for the ice particles in the stratiform shield show a relationship with height/temperature (Fig. 4c). At lower altitudes (higher temperatures), the distribution is broader based on the concentration of larger particles in the PSD. At higher altitudes (lower temperatures >~7 km ASL), the PSDs are narrower and all particles are smaller than 4 mm. In the anvil outflow, the temperatures are all less than -20° C. However, the PSDs are relatively broad and contained larger particles (>4 mm). The PSDs also show more larger particles at lower altitude. The coldest legs have the highest concentration of small particles (<1 mm).

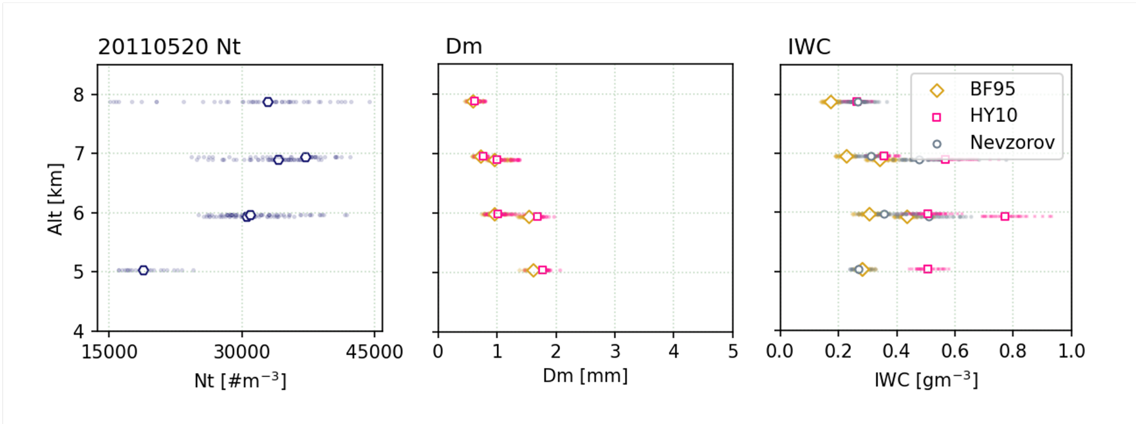

Fig. 5. Summarizing the number concentration (N_t) for all ice particles with D > 150 μm, mass-weighted mean diameter (D_m) and ice water content (IWC) from the convective line event (20 May 2011). Unfilled-markers show the median values for each variable, while all of the observations are included as smaller, filled-in markers. The D_m and IWC are calculated using the OAP PSDs and mass-dimensional relationships indicated as HY10 and BF95 for Heymsfield et al. (2010) and Brown and Francis (1995). The TWC from the Nevzorov probe is also included for additional comparison.

1) Convective Line Stratiform Shield: 20 May 2011

Figure 5 summarizes the values of N_t, mass-weighted mean diameter (D_m) and ice water content (IWC) for the ice particles with D > 150 μm in the trailing stratiform shield region using the HY10 and BF95 m-D relationships. Above the melting level, there is a general decrease in particle concentration and increase in particle size with decreasing height. At ~8 km ASL, the median D_m is 0.6 mm and increases to 1.7 mm below 6 km ASL. At lower levels, where the particles are larger, the D_m values for HY10 are larger than BF95 by 0.16 mm. At all altitudes, the IWCs from HY10 exceed the BF95 values. The BF95 IWC values have a smaller range between 0.17 and 0.43 gm^{-3} depending on altitude, while HY10 IWC values are sensitive to the increase in particle size as IWC values range from 0.26 to 0.77 gm^{-3}.

The N_t values from each leg are separated by habit category in Fig. 6. The N_ts for spherical, linear, and irregular habits increase with altitude, with the smallest values generally located near the melting level. At higher altitudes (6-8 km ASL), there are thousands per m^{-3} of small spherical, linear, irregular particles, but below 6 km ASL, the N_t of these habits are greatly reduced. These particles are primarily smaller in size and the larger particles occur at lower altitudes. While there

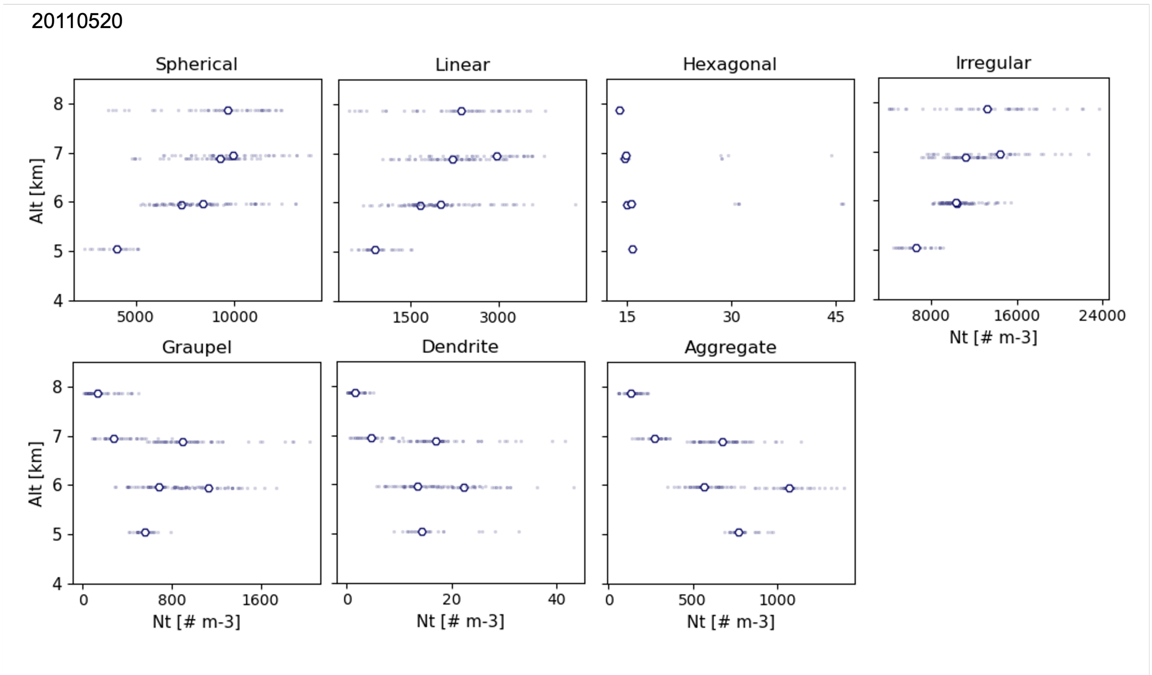

FIG. 6. The number concentration (N_t) [#m^{-3}] for each UIOOPS particle type for D > 150 μm on 20 May 2011. Unfilled-markers show the median value for each subset/leg, while all of the observations are included as smaller, filled-in markers. The N_ts can vary by orders of magnitude between particle habits, so each particle type is plotted separately with unique x-limits. The irregular particle type also includes particles that are too small to sort into any category.

is inherent uncertainty in any habit identification, there are features of the particles observed by the OAPs that are consistently changing with altitude. The aggregate category has an increasing N_t with decreasing altitude. At ~8 km ASL, there are fewer than 500 m^{-3} of aggregates, but at ~6 km ASL, the N_t values exceed 1500 m^{-3}. As the particles fall, they aggregate and produce larger particles and larger reflectivities. The graupel category also increases with decreasing altitude. These results are consistent with dual-polarized radar observations, Dolan et al. (2022) show increasing aggregates toward the melting level. The dendrite and hexagonal categories both contain very low N_t throughout this event, but it is noted by Schima et al. (2024) that it is difficult to differentiate these habits in OAP decision tree analysis.

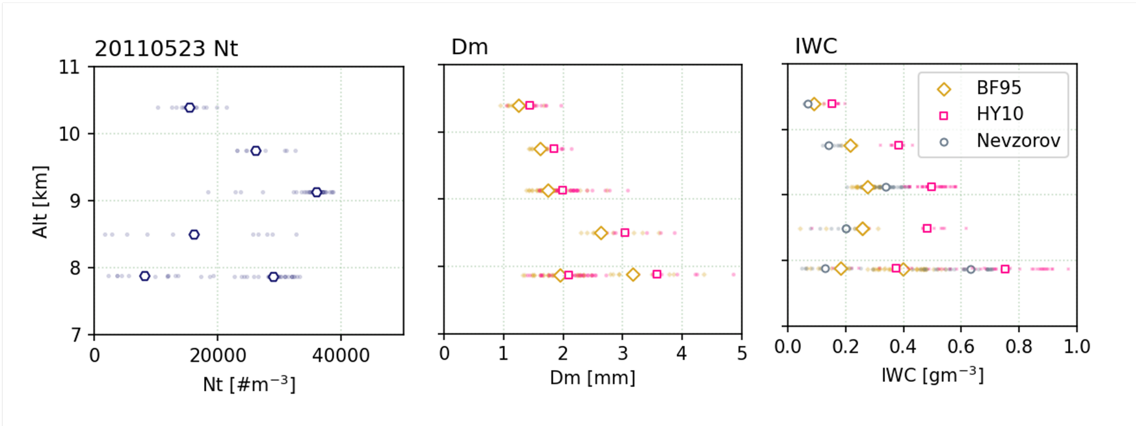

FIG. 7. Same as Figure 5 for supercell anvil outflow (23 May 2011)

2) SUPERCELL ANVIL OUTFLOW: 23 MAY 2011

The Citation sampled a range of ice particles between ~8 to 10.5 km ASL in the anvil outflow of the storm. Figure 7 shows the values of N_t, D_m and IWC for all collocated legs. In Fig. 4, the mean PSDs show an indication that there are more small particles at higher altitudes, however, Fig. 7 shows that there is a less systematic relationship with height and N_t below 9 km. On the other hand, there is a clearer change in D_m with height; the D_ms increase with decreasing altitude. The median D_m at 10.4 km ASL is near 1.4 mm with HY10 and slightly larger than BF95, while the HY10 D_m increases to 2 mm at ~9 km ASL. Median values reach as high as 3.6 mm at 8 km ASL, but the range exceeds 4 mm. For all legs, the HY10 IWCs are larger than the BF95 values. For the following IWC discussion, the values are reported for HY10 only. There is an increase in IWCs with decreasing altitude: 0.15 g m^{-3} at 10.4 km ASL increasing to 0.75 g m^{-3} just below 8 km ASL. However, there are also two Citation legs with slightly lower values of IWC of 0.48 and 0.4 g m^{-3} at 8.5 and 8 km ASL, respectively. The increase in D_m and IWC with decreasing altitude is consistent with size sorting in the anvil outflows, with larger and more massive particles falling to lower altitudes. At ~8 km, the two legs are dissimilar in the N_ts, D_ms, and IWCs, which is likely from sampling different parts and time of the anvil outflow (fig. not shown).

There are relatively high N_t values for spherical, linear and irregular categories at most altitude legs sampled by the Citation (thousands of particles) compared to the other habits. Similar to the stratiform shield following the convective line, the hexagonal and dendrite categories were not highly observed (low N_t < ~60 m^{-3} for all altitude legs), but there are known challenges in

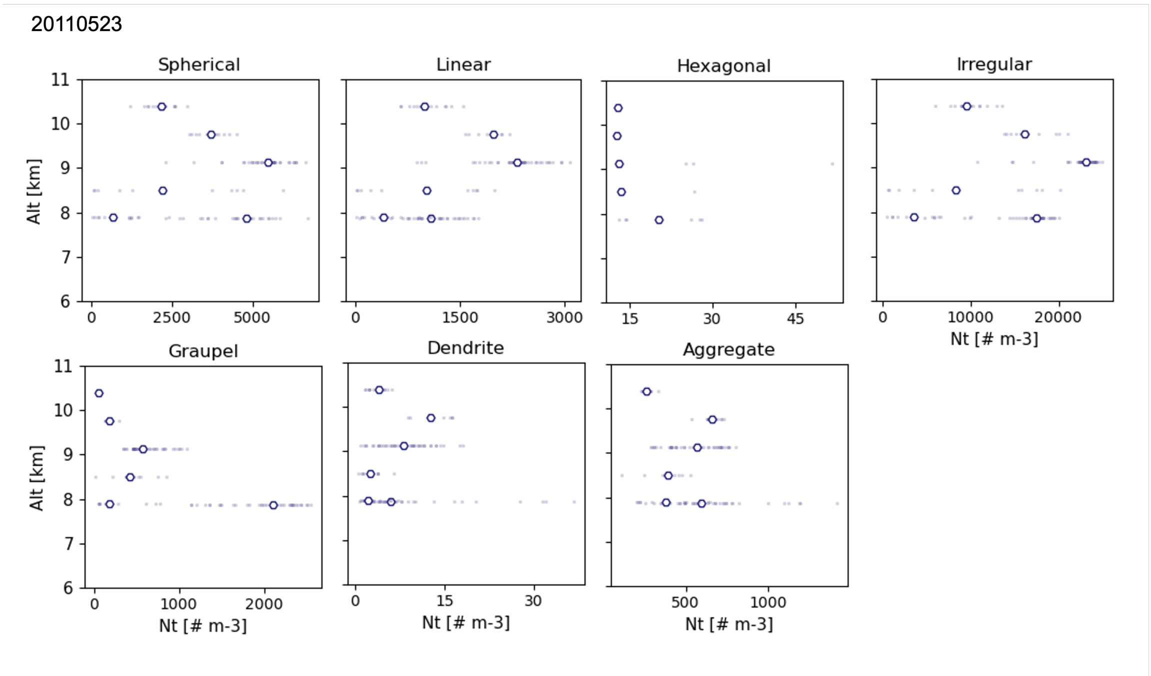

FIG. 8. Same as Figure 6 for supercell anvil outflow (23 May 2011)

identifying these habits in the OAPs (Schima et al. 2024). The aggregate category is observed at all altitudes sampled by the Citation, however, the N_t values are lower than for the other categories. There is a maximum number of aggregates at 8 km ASL. One of the legs at 8 km ASL has notably more graupel particles with N_t values exceeding 2000 m^{-3}. Unlike the stratiform shield, the observations from the anvil outflow appear more variable throughout the altitudes sampled, which may possibly be due to differences within the anvil regions and timing of the flightpath.

b. Remote Sensing and Forward Modeling

This subsection compares radar observations with forward modeled reflectivities, beginning with a detailed flight leg example from each event. Forward modeled reflectivities are based on the habit mixtures (HX) that are documented in Table 1. In the forward modeled reflectivities shown for the following detailed examples, the HX combination includes a lightly rimed aggregate particle (Leinonen15A01) in the graupel category. In the following sections, the HX reflectivities use the same particle mixtures, but the aggregate category is varied by riming amount (Table 1).

1) Detailed Example: Convective Line Stratiform Shield (20 May 2011)

In Figure 9, the PSDs, HIWRAP Ka-band reflectivities and simulated Ka-band reflectivities are shown for one segment observed at approximately 1430-1440 UTC. The Citation and ER-2 overlap in time and sample the same region within the stratiform shield (Fig. 1). At 6.9 km ASL (-16.45° C), particles are relatively small (D<4 mm) with a high concentration at D less than 1 mm (Fig. 9a). The distributions of the small particles include spherical, linear, and irregular habits (Fig. 9b). Particles with D > 2 mm are mostly represented in the irregular, graupel and aggregate categories. In this flight segment, there are notably high numbers of small particles with relatively fewer aggregates and graupel particles, and we surmise that particles have not yet fallen a sufficient depth through the cloud to aggregate together. There is a visible discontinuity in the plots of D versus time around a value of ~1 mm in the habit PSDs; this gap in the PSDs results from blending data from two separate probes that observe particles at different sizes and bin resolutions.

The HIWRAP Ka-band observations are shown in Fig. 9c. The cloud echo top heights (CTHs), defined by the altitudes where reflectivities are less than -5 dBZ, are approximately 10 km ASL. The reflectivities gradually increase towards the apparent melting layer at ~4 km ASL. Figure 9d shows normalized distributions for HIWRAP and forward modeled reflectivities. At the Citation altitude, the HIWRAP Ka-band reflectivities range from 6 to 11 dBZ with most values at 9 dBZ. The forward modeled particle/habit mixture (labeled as 'HX') reflectivities show a range of reflectivities depending on the amount of assumed riming on the aggregate category. The modeled reflectivities can differ from the HIWRAP observations by more than 10 dB (under and overestimate) as the riming on aggregate particles varies. The distribution of the HIWRAP reflectivities is between the modeled reflectivity distributions for the Ze_HX_02 and Ze_HX_05 mixtures, for which the aggregate riming groups are differentiated by the ELWP of 0.2 kgm^{-2} and 0.5 kgm^{-2}, respectively. In addition to the forward modeled HX reflectivities, the figure shows the reflectivities calculated using the HY10 and BF95 mass-dimensional relationships. The HY10 reflectivities agree well with the HIWRAP reflectivities, while the BF95 reflectivities underestimate the observed reflectivities.

2) Detailed Example: Supercell anvil outflow (23 May 2011)

Figure 10 summarizes a detailed example of in-situ microphysics and remote sensing observations of the supercell anvil flow observed on 23 May from ~2251 to 2303 UTC. The Citation and ER-2

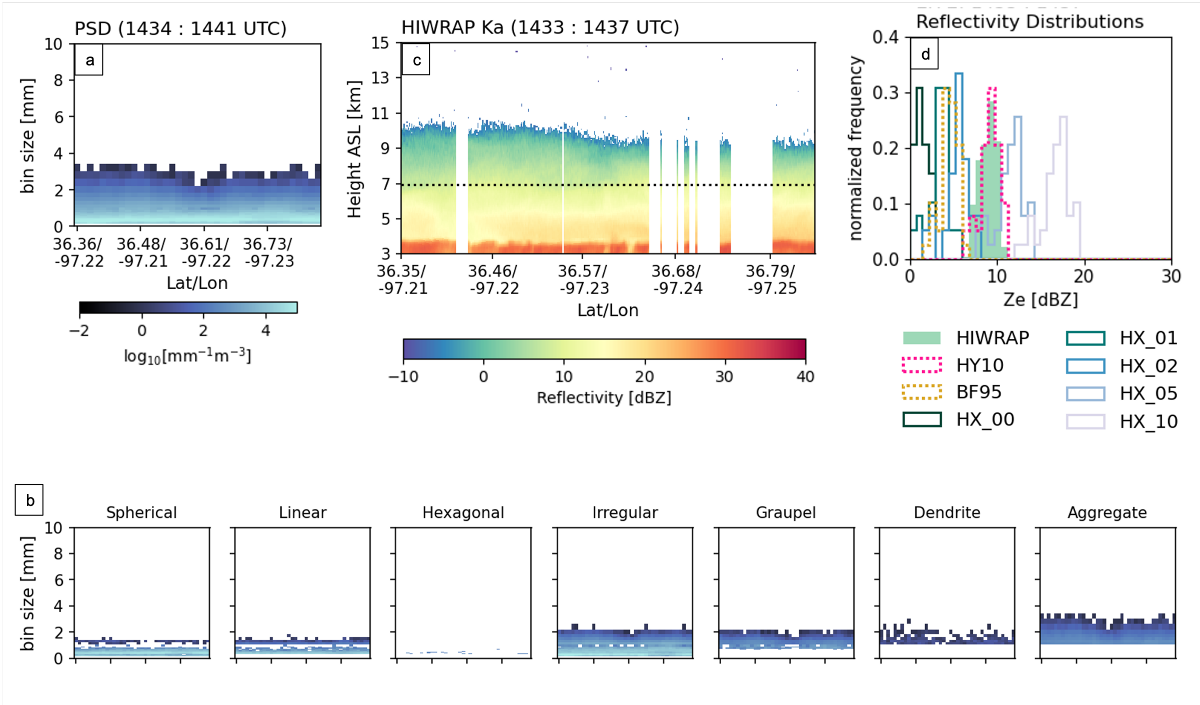

378 Fig. 9. Example subset of microphysics and remote sensing observations on 20 May 2011. The subplots include: (a) in-situ particle size distribution, (b) detailed habit PSDs, (c) HIWRAP Ka-band reflectivities, (d) distribution of reflectivities. HIWRAP observations are masked for aircraft turning (roll). The black dotted in (c) indicates the mean height of the Citation. The reflectivity distributions include HIWRAP and forward modeled reflectivities for varying aggregate category with increasing riming from the snowScatt database. The legend includes the equivalent liquid water path value from 0.0 kgm^{-2} to 0.5 kgm^{-2}. This subset of in-situ microphysics and radar observations correspond to the NEXRAD and GOES shown in Fig. 1.

sampled anvil clouds repetitively (Fig. 2) in a bow-tie pattern (full flight-path patterns not shown). The in-situ leg was flown at ~9.1 km ASL (-34.4° C). The PSDs show large particles exceeding 6 mm (Fig. 10a). Similar to the conditions within the stratiform shield, there is a high concentration of small particles from the spherical, linear and irregular categories and larger particles included in the irregular, graupel and aggregate categories (Fig. 10b). The irregular particle sizes do not exceed 5 mm. Particles categorized as graupel are as large as 7 mm. The largest particles observed by the HVPS in this anvil cloud region are in the aggregate category with particles exceeding 7 mm.

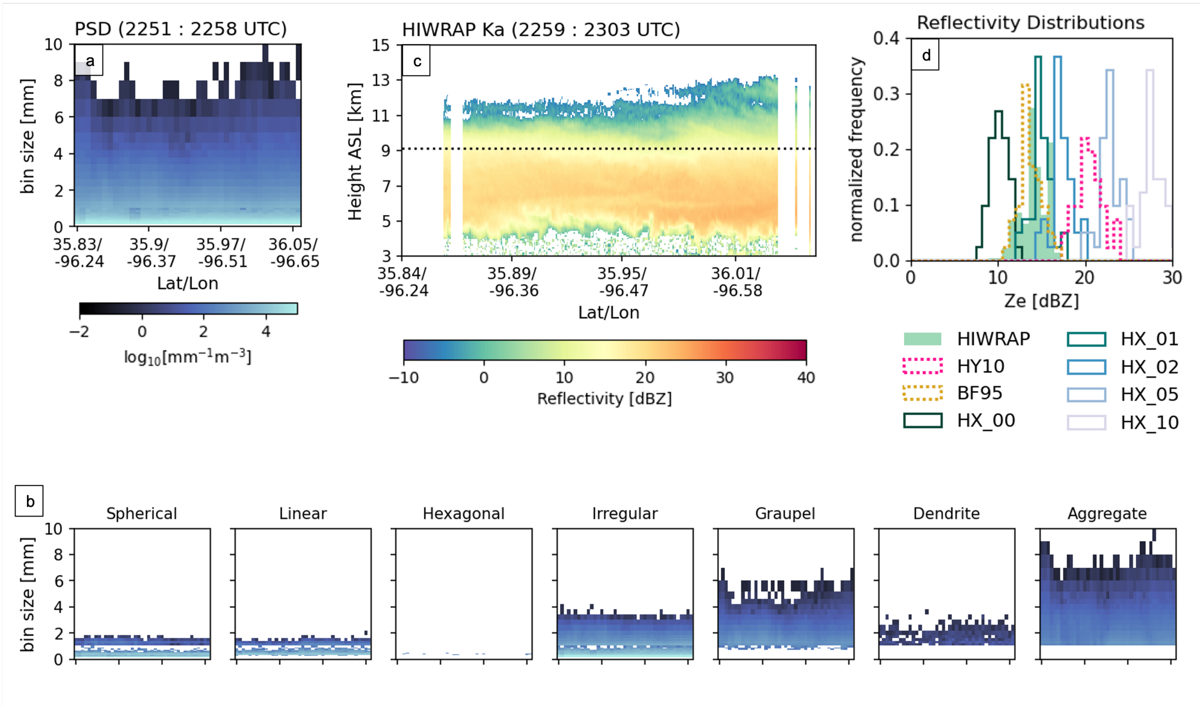

FIG. 10. Same as Fig. 9 for 23 May 2011. This subset of in-situ microphysics and radar observations correspond to the NEXRAD and GOES shown in Fig. 2.

The HIWRAP Ka-band observations show CTHs exceeding 11 km ASL with reflectivities near 0 dBZ (Fig. 10c). The reflectivities increase with decreasing height, but below ~5 km ASL the reflectivity drops quickly, perhaps due to sublimation. The HIWRAP Ka-band reflectivities at the mean Citation height ranged from 9 to 16 dBZ, with the most of the reflectivities at 14 dBZ (Fig. 10d). The forward modeled HX reflectivities show a range of reflectivity distributions, with a high degree of sensitivity to the different amounts of riming on the aggregate categories. Reflectivities can be underestimated and/or overestimated by as much as 10-20 dBZ. The mixture of particles that use a lightly rimed aggregate (Ze_HX_01) agrees well with the HIWRAP observations. Reflectivities calculated using the HY10 and BF95 mass-dimensional relationships are included in the distributions; the BF95 mass-dimensional relationship produces reflectivities comparable to the HIWRAP, in contrast to the stratiform shield distributions (Fig. 9d).

c. Summarizing Radar: Observed and Forward Modeled

Figures 11 and 12 summarize the ER-2 HIWRAP radar observations in two-dimensional (2D) histograms, and the synthetic radar reflectivities and DFRs are shown for each altitude all of the riming particle mixtures (Table 1). The analysis starts with the stratiform shield (Fig. 11), followed by the anvil outflow (Fig. 12).

1) Convective Line Stratiform Shield (20 May 2011)

In the stratiform shield region above the melting level, the HIWRAP Ka-band reflectivities gradually increase from -10 dBZ at 11 km to ~20 dBZ above the melting layer at ~4 km ASL (Fig. 11a,c). Citation observations of ice microphysics occur between 5 km ASL and 8 km ASL, which feature a reflectivity increase from 0 to 20 dBZ. The increase in reflectivity towards the melting level supports the occurrence of aggregation. The number concentration of aggregates observed by the OAPs also increases with decreasing height from 8 to 4 km ASL (Fig. 6). The DFRs increase towards the melting level as the ice particle sizes increase (Fig. 11b,d). Figure 5b shows an increase in the D_m with decreasing altitude, and Fig. 4c shows the broadening distributions with lower altitude/warmer temperature. Above 7 km ASL, the 2D histogram shows the occurrence of counts of large (negative and positive) DFRs associated with lower reflectivities, which are artifacts of observing the cloud edge where the observed reflectivity is nearing the Ku-band noise floor.

In addition to the HIWRAP Ka and DFR observations, Fig. 11 summarizes the forward modeling results for the aggregate riming and graupel tests with markers for each median distribution. Figure 11a,b present the results from the first graupel test, in which the graupel particle is specified to be a lightly rimed aggregate (Leinonen A01). The simulated reflectivities span both lower than and greater than the observed HIWRAP values through the simulated HX reflectivities. For example, at 7 km ASL the HIWRAP measured reflectivities between 5 and 15 dBZ, but the separate riming tests show that the forward modeling can result in values of ~0 dBZ up to ~21 dBZ depending on the riming on the aggregate particle. The simulated DFRs are low at the higher altitudes where there are primarily small particles, but there is a gradual increase with decreasing height, which corresponds to the increasing particle size. Also, at each given altitude leg, the DFR values increase with riming on the aggregate particle, so the DFR is sensitive to the mass on the same equivalent particle size, especially for lower altitudes. At 5 km ASL, the DFR for HX_00 is

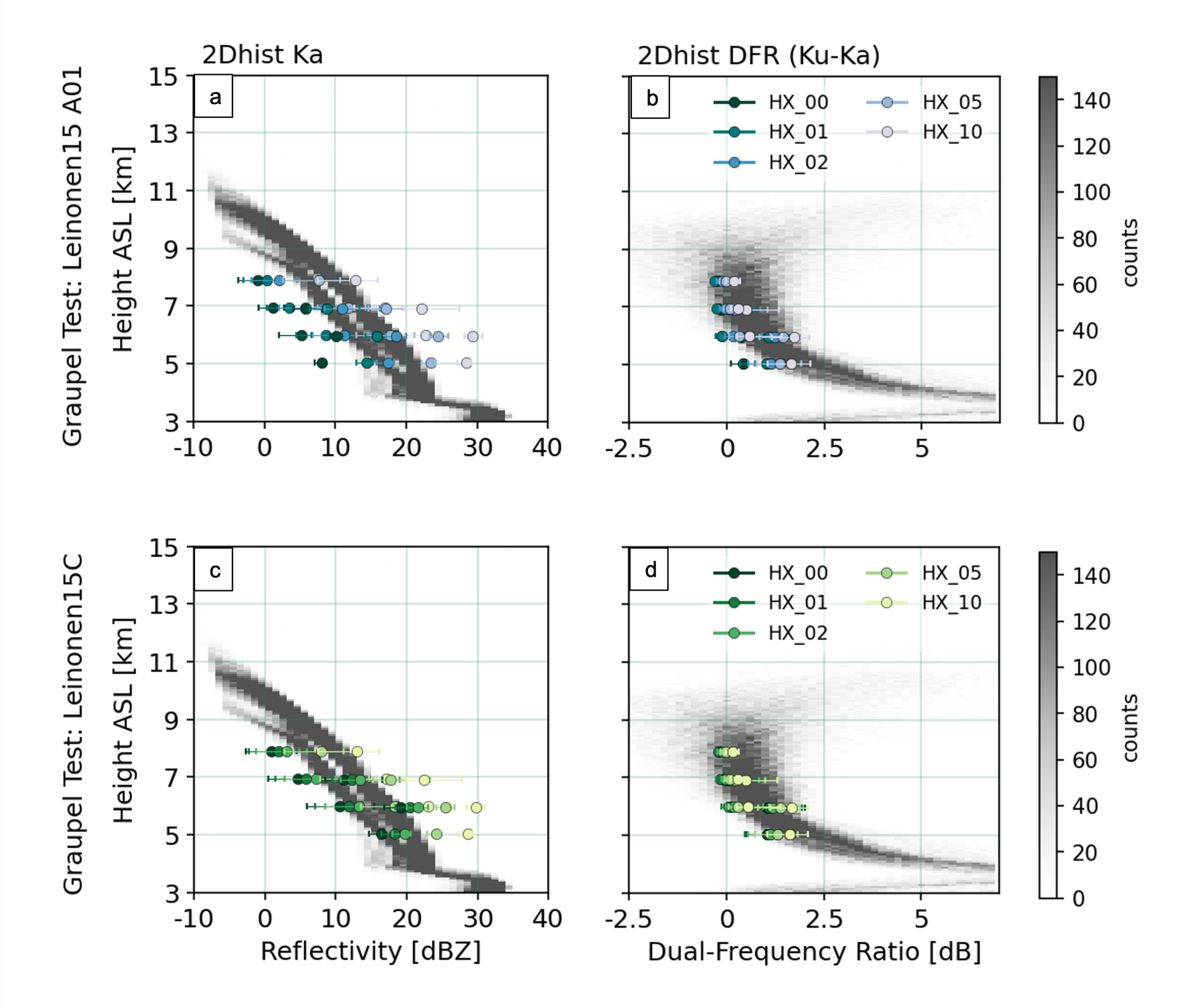

FIG. 11. Two-dimensional histograms of Ka-band Radar Reflectivities (a,c) and Dual-Frequency Ratios (b,d) for 20 May 2011. The grayscale colormap shows the counts of observations from the HIWRAP in the 2D histogram. For 20 May 2011, there are 4 distinct HIWRAP subsets and there are 6 Citation separate PSD series. Each particle mixture is shown with a different color based on the riming of the aggregate category. The top plots (a,b) include simulated Ka-band reflectivities and dual frequency ratios. The circle markers show the median of the reflectivity (and DFR) distribution for the microphysics subset. The horizontal lines span the range of reflectivities with the minimum and maximum at the endpoints with small vertical line markers.

near 0.5 dB, while the HIWRAP observations are greater than 1 dB. The HX reflectivities with additional riming improve agreement with the HIWRAP DFRs.

Results from the second graupel test (Leinonen C) are shown in Fig. 11c,d. Above 7 km ASL, the HX distributions are similar to Fig. 11a because there are few graupel particles to influence the total reflectivity (Fig. 6). Below 6 km ASL, there are higher concentrations of graupel and aggregates, which contribute to higher reflectivities for the separate HX simulations. Especially for the two lowest altitude legs (~5 km and ~6 km), the forward modeling shows how the reflectivities increase in response to the denser graupel particle. This change is larger for the HX groups with less riming on the aggregates. To highlight one of the legs: at ~5 km ASL, the median Ze for HX_00 in Fig. 11a is 8 dBZ while in Fig. 11c, the median Ze for HX_00 is increased to 16 dBZ. On the other hand, the median Ze for HX_05 only increases 1 dB from 23 dBZ to 24 dBZ. In the graupel tests (Fig. 11b,d), the simulated DFRs have little differences.

2) Supercell anvil outflow (23 May 2011)

In Fig.12a,c, the radar reflectivities of the anvil outflow show that CTHs are higher for the anvils than for the stratiform shield clouds from the previous day, with reflectivities near -5 dBZ at ~13 km ASL. These high CTHs are also consistent with the low brightness temperatures (< 215 K) associated with the widespread anvils observed in the GOES water vapor channel (Fig. 2a). The reflectivities increase fairly quickly from -5 to 10 dBZ from 13 km ASL to 11.5 km ASL. Then, with decreasing height from 11 to 5 km ASL, the reflectivities gradually increase to 25 dBZ. Below 5 km, the reflectivity counts lower, again possibly due to ice particle sublimation. The DFRs increase with decreasing height, which supports the occurrence of size sorting (and aggregation) as larger particles are lower in the depth of the cloud (Fig.12b,d). In addition, there are also areas of enhanced DFRs above 7 km ASL. These high DFRs indicate variations in the anvil cloud vertical structure and spatial variations as the ER-2 observes the anvil outflow. Between 5-7 km ASL, the reflectivities show little change with decreasing height, while the DFRs continue to increase (the Ku-band reflectivities are increasing). Effects from non-Rayleigh scattering and attenuation can impact the radar reflectivities at these heights (Jensen et al. 2016; Tridon et al. 2019). In the Ka-band, large particles can lead to non-Rayleigh scattering (Matrosov et al. 2019; Tridon et al. 2019), which would result in lower reflectivity values. While attenuation in ice is generally less than in liquid profiles, there may still be effects of attenuation on the profile. Simulated extinction coefficients for particles above 7 km ASL are very small in the Ku-band with values near

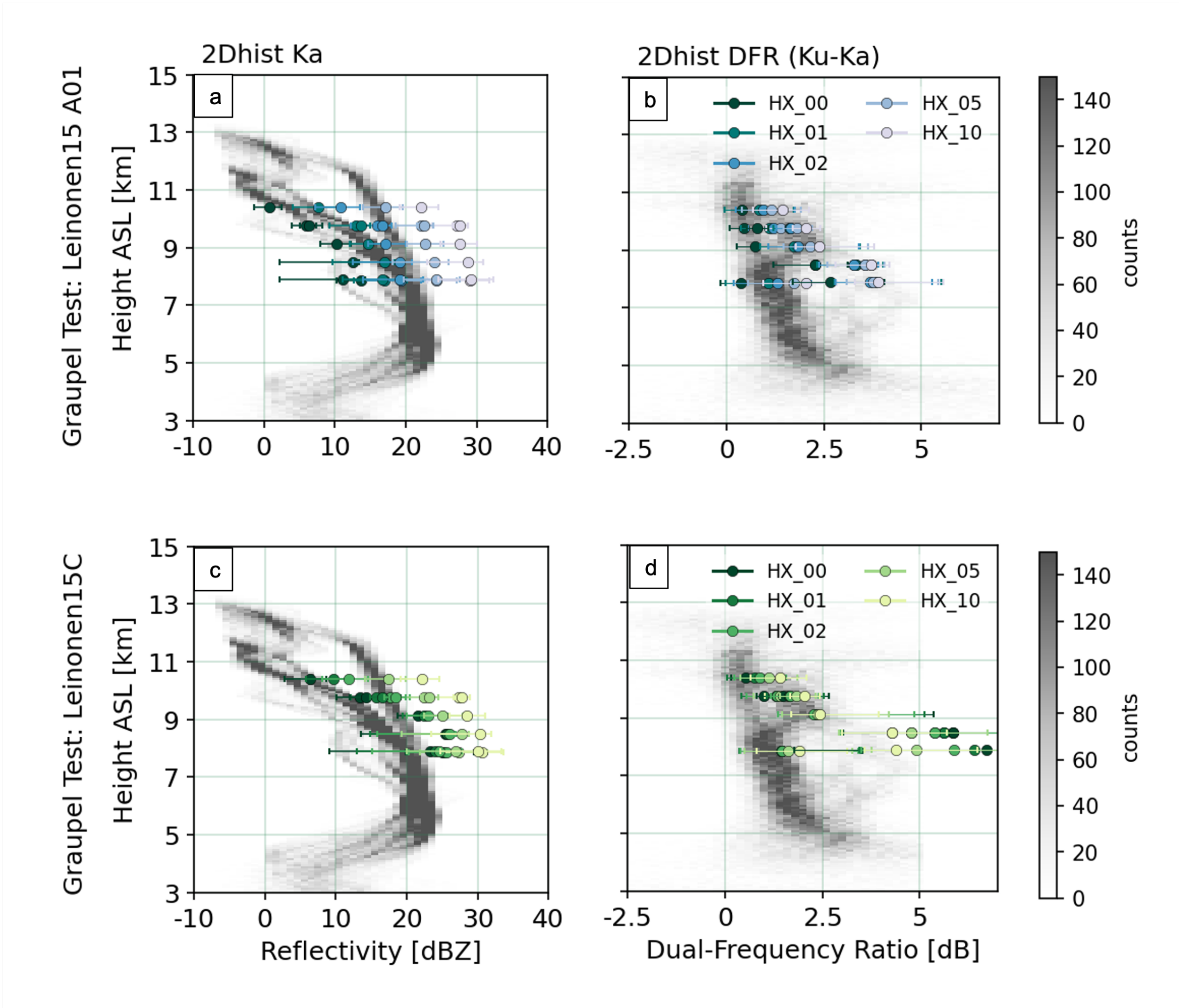

FIG. 12. Same as Fig. 11 for 23 May 2011. There are 5 distinct HIWRAP subsets and there are 6 Citation legs.

0 dB km^{-1}figure not shown). In the Ka-band, the simulated extinction coefficients range between 0.01 to 1 dB km^{-1} depending on the aggregate riming assumptions (higher extinction coefficients for mixtures with more riming on the aggregate particles). In addition, between 5-7 km ASL the temperatures range from -10 to -20° C (Fig. 4), which suggests there may be mixed-phase conditions where liquid phase particles would result in additional attenuation on reflectivities particularly at Ka-band.

The forward modeled HX reflectivities and DFRs for the aggregate riming and graupel tests are shown on the top and bottom panels of Fig.12. In particular, HX_01 and HX_02 agree with the range of HIWRAP observations for most of the altitude flight legs with the lightly rimed aggregate used in the graupel category (Fig. 12a). In the second graupel test, where graupel PSDs are LeinonenC graupel particles, the reflectivities are too high compared to the HIWRAP, especially between 8.5 and 9 km ASL, where the distributions of reflectivities exceed the range of any of the profiles observed (Fig. 12c). Similar to the forward modeled reflectivities from the stratiform shield ice particles during 20 May (Fig. 11a,c), the graupel test has a more notable impact on the ranges of reflectivity produced by different HX with less aggregate riming. The 8.5 km leg illustrates the impact of the graupel particles on the HX reflectivities: for HX_00, the median reflectivity in graupel test 1 (less dense graupel; Fig. 12a), is 12.5 dBZ, and in graupel test 2 (LeinonenC; Fig. 12c), the median reflectivity is 25 dBZ. For HX_02, the median reflectivity in graupel test 1 is 24 dBZ, and is 28 dBZ in graupel test 2. At 8.5 km ASL, the HIWRAP reflectivities are concentrated between 15 and 22 dBZ.

The forward modeled DFRs span the HIWRAP observations fairly well when the graupel category is assumed to be a lightly rimed aggregate (Fig. 12b). For graupel test 2 (Fig. 12d), the HX DFRs are similar to graupel test 1 (Fig. 12b) for the Citation legs above 10 km ASL. However, the forward modeled DFRs below 10 km ASL overestimate HIWRAP DFRs in graupel test 2. In addition, these cases have larger particles observed at higher levels (Figs. 7, 4) compared to the stratiform shield case, and this is notable in higher DFR values in the HIWRAP and forward modeled HX DFRs. Below 9 km ASL, the HX groups show a distinct pattern for several legs where the highly rimed groups (HX_10) have lower DFRs than less rimed groups. This can be seen in the pattern of light yellow/green median markers left of the darker median markers (altitude leg 8.5 km ASL). This shows that an increase in the riming/mass on the aggregate category reduced the relative difference between forward modeled Ka and Ku-band reflectivity.

3) Vertical Motions

The Doppler velocities in Figure 13 encompass a measure of the air motion and hydrometeor fall-speeds. The positive (negative) values indicate downward (upward) motion of clouds/precipitation. The Doppler velocities in the stratiform shield show a gradual increase with decreasing altitude (Fig 13a) consistent with aggregation, size sorting, and finally melting hydrometeors. The values increase from ~0.5 at 9 km ASL to ~2 ms^{-1} right below 5 km ASL. The sudden increase in Doppler velocity at ~4 km ASL corresponds to the melting level.

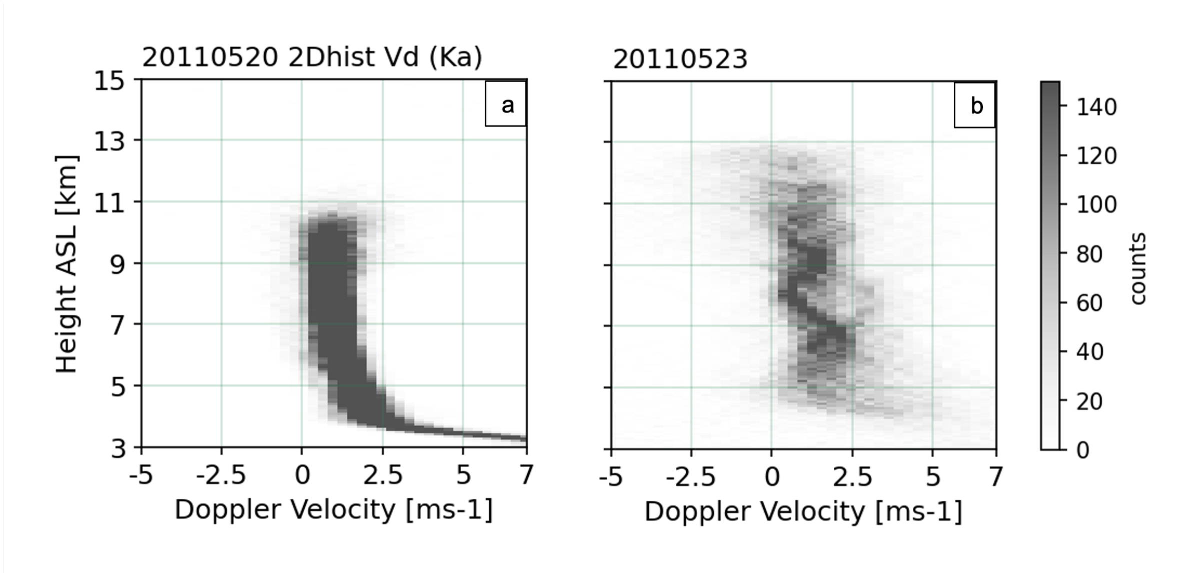

FIG. 13. Two-dimensional (2D) histograms of HIWRAP Ka-band Doppler velocities. Stratiform shield (left) and anvil outflow (right).

In the anvil outflow, the Doppler velocities show an increase with decreasing altitude (Fig 13b). However, in contrast to the stratiform shield, the vertical motions in the anvil outflow are more variable throughout the profiles. Upward motions are observed at all heights, though this feature is more pronounced at some heights. Between the CTH (~13 km ASL) and 9 km ASL, the Doppler velocities range from -2 ms^{-1} to 2.5 ms^{-1}. The upward motions are weaker below 9 km ASL, with the majority of the observations between 0.5 and 3 ms^{-1}. Below 7 km ASL, the distribution of Doppler velocities broadens further to include observations of nearly 4 ms^{-1}. The large range of values including upward and downward motions indicate the turbulent motions in these clouds. Vertical wind measurements from the Citation also show variability in vertical motions from -10 to 5 ms^{-1} during the flight (Fig. not shown). In contrast, the vertical winds in the stratiform shield case, the values ranged from -2.5 to 2.5 ms^{-1}. Ground-based observations at the Department of Energy (DOE) Atmospheric Radiation Measurement (ARM) facility from a Ka-band ARM Zenith Radar (KAZR; not shown) also illustrate similar characteristics of Doppler velocities from observations of the stratiform shield and anvil outflows.

The Doppler velocities combined with the DFRs provide insights into the processes occurring in the anvil outflow and stratiform shield. In the stratiform shield layer, the DFRs and Doppler velocities steadily increase towards the surface indicating particles growing by aggregation as they fall - and falling faster with size and mass. The N_ts and D_ms also show that with increasing size there are fewer particles (Fig. 5). The combination of in-situ and remote sensing observations support the occurrence of aggregation above the melting layer. In the anvil outflow, there is an increase in DFRs and Doppler velocities with decreasing height indicating size sorting and aggregation as well (Fig. 7). However, there are also enhanced DFRs at higher levels and large particles (Fig 12). The Doppler velocities show upward movement and substantial variability in the anvil outflow suggesting that vertical motions may loft larger particles upward.

4. Discussion

a. Unique events

The analysis of in-situ microphysics and remote sensing observations highlights two unique storm regimes from MC3E in the same geographic region separated by a few days. The convective line stratiform shield (20 May) primarily featured observations of ice particles falling above the melting level and the trailing ice clouds at the end of the storm. The reflectivities, Doppler velocities and DFRs increase toward the melting level, and the PSDs broaden to include larger sizes with increasing relative number of aggregates. These variables suggest ice particle aggregation as the particles fall through the cloud depth. In general, the PSDs in the supercell anvil outflow (23 May) contained larger particles compared to the stratiform shield, with numerous large aggregate particles at higher and colder levels. The deep convective cells resulted in anvil outflows with CTHs extending to 13 km ASL (Fig. 12). Increasing reflectivities, Doppler velocities, and DFRs with decreasing altitude also suggest the occurrence of aggregation and size sorting. However, enhanced DFRs at higher levels and the upward Doppler velocities in the anvil outflow possibly support vertical motions lofting large particles higher levels.

b. Sensitivity to Habit

There are numerous combinations of particle scattering (and mass-dimensional) properties that can be used to find agreement with aircraft radar observations. The UIOOPS criteria were used to inform the types of particles simulated for each category. While there are inherent uncertainties in particle identification (Schima et al. 2024), the particle descriptions provide an input for habit type and decisions for forward modeling that we then assess by comparing the range of simulated reflectivities against observed reflectivities. In addition, the habit categories combined with the D_m values and radar reflectivity profiles provide additional insights to inferred processes such as aggregation. Some particle choices have a larger impact on the reflectivity. In general, PSDs with smaller particles were less sensitive to the type of particles used in simulating reflectivity with exceptions such as solid ice spheres, which have a high impact on reflectivities resulting from the large m-D exponent (figure not shown). The graupel and aggregate categories, which are represented by larger particles, were sensitive to the riming assumptions from the databases.

Changes to the graupel and aggregate characteristics have large effects on the forward modeled reflectivities which span a range of ~20 dB depending on the amount of riming. Although the supercell event (23 May) had been documented to have hail (Heymsfield et al. 2013b), the use of the dense graupel particle (LeionenC) to forward model the microphysics in the anvil outflow leads to reflectivity overestimates. The simulated anvil reflectivities are more aligned with the HIWRAP observations when the graupel particles are represented as aggregates (Fig. 12). The detailed example of a collocated segment of remote sensing observations in Fig. 10d shows agreement of HIWRAP observations and BF95 reflectivities. The BF95 mass-dimensional relationship implies less mass for a given particle size compared to HY10 (Fig. 3). This supports the assertion that the particles are less dense for a given aggregate and graupel particle, but when assuming a lower m-D graupel particle, some riming is needed for the reflectivities to be consistent with those that were observed.

In the stratiform shield following the convective line, changes in the riming assumption on the aggregate particles lead to variations in forward modeled reflectivities of ~20 dBZ. In particular, denser particles are needed at lower altitude legs in order for simulated reflectivities to be consistent with the observations (Fig. 11). In general the DFRs were insensitive to the graupel type, but responded substantially to the aggregate riming. In contrast to the anvil outflow, the stratiform shield example matched well with the HY10 reflectivities (Fig. 9d), which implies a higher IWC content (Fig. 3, 5). While dense graupel particles were not necessarily likely to form in the stratiform shield layer (fairly invariable vertical wind speeds, no icing detection of supercooled liquid from the Citation observations), the results indicate that a higher mass/IWC was needed to realistically forward model the reflectivities. The Nevzorov probe was used for measurements in the MC3E, but is known to underestimate total water content and IWC (Korolev et al. 2013; Wang et al. 2015), which makes it difficult to use these in-situ observations to assess the bulk IWC.

c. Broader Connections

Various studies have investigated characteristics of anvil and stratiform clouds in convective environments, which provide additional context for these MC3E results. Bouniol et al. (2010) characterized properties of anvils from deep convection in West Africa using W-band and in-situ observations. They found rimed aggregates were the predominant particle in 2DC observations from the stratiform anvil region. They also compared computed reflectivities from BF95, and found an underestimate compared to the observed W-band. In the CRYSTAL-FACE campaign (Cirrus Regional Study of Tropical Anvils and Cirrus Layers [CRYSTAL] Florida Area Cirrus Experiment [FACE]), Heymsfield et al. (2004) used in-situ observations to assess ice particle density and found rimed aggregates in convectively generated cloud regions. Stechman et al. (2020) used aircraft in-situ and radar observations from the BAMEX (Bow Echo and Mesoscale Convective Vortex Experiment) and PECAN (Plains Elevated Convection at Night) to analyze hydrometeor characteristics in different parts of MCSs. They show aggregation was observed in all of the zones (transition zone, enhanced stratiform region, and anvil regions), and they note that environmental conditions (relative humidity) affect the sublimation and aggregation processes. Results presented here in this study and in previous papers emphasize the prevalence of aggregates in clouds associated with convection- and the need to also explore riming on cloud particles.

The utility of multi-frequency and multi-measurement perspectives have also been highlighted in several field campaign studies. Using in-situ and aircraft radar observations from multiple field campaigns (including MC3E), Duffy et al. (2021) show that relationships between D_m and DFR are more effective for retrieving D_m compared to relationships between the reflectivity and D_m, and that the empirical DFR-D_m relationships vary with temperature. The IMPACTS (Investigation of Microphysics and Precipitation for Atlantic Coast-Threatening Snowstorms; McMurdie et al., 2022) field campaign featured collocated in-situ and multi-frequency radar observations of winter storms. Finlon et al. (2022) use DFRs (X, Ku, Ka, W) and in-situ observations from IMPACTS to evaluate a preexisting neural network radar retrieval Chase et al. (2021), and found that the combination of observations and retrievals can be used to infer microphysical processes. Heymsfield et al. (2023)

assessed relationships between four radar wavelengths (X, Ku, Ka, W) and ice microphysical properties including PSDs, D_m and IWC in the context of different particle models (e.g. T-Matrix, SSRGA), and found differences in the impact of the particle representation on reflectivities and describe that SSRGA methods adequately simulates reflectivities. Tridon et al. (2019) use triple-frequency (Ku, Ka, W) radars with airborne in-situ observations from the Olympic Mountains Experiment (OLYMPEx) to relate particle mass/size and DFRs to particle type and processes. They compare forward modeled reflectivities for SSRGA aggregates to find agreement with varying amounts of riming assumptions along coordinated flight legs in stratiform systems. Additional measurements of vertical motions and icing allowed them to directly connect the SSRGA rimed aggregates to reflectivity increases resulting from increased riming along the flight legs.

5. Conclusions

In this study, MC3E field campaign observations of in-situ probe and radar remote sensing data were used in concert with a radar forward model to explore the relationships between microphysical properties and radar reflectivity. PSDs and habits were obtained from processed optical array probe data. The habit categories were used to inform the assumed ice crystal shape and degree of riming in simulation of reflectivities, and several forward model tests were evaluated using various ice particle habit mixtures. While the two cases explored in this study were only a few days apart and in the same region, the storm systems were distinct and provide a separate look into the stratiform region following a convective line (20 May), and anvil flow from supercell convection (23 May). Ice particle characteristics, environmental conditions, and the radar observations are presented to provide a multi-measurement perspective on these distinct convective events.

Combining the in-situ microphysical observations with the remote sensing variables highlights the utility in multi-measurement perspectives, and deepens our understanding of ice phase particles and anvil clouds. Processes such as aggregation were inferred in the stratiform region and anvil through the PSDs, habit-specific Nt, and changes in the reflectivities, DFRs, and Doppler velocities. The DFRs are sensitive to the change in particle size with decreasing altitude. In addition, HIWRAP Doppler velocities also suggest upward vertical motions in the anvil outflow, which may loft larger particles upward.

Forward modeled radar reflectivities from different particle mixtures were compared to HIWRAP reflectivities and DFRs (Ku-Ka). The simulations tested the impact of increasing the riming on the aggregate particles, and the impacts of using a lightly rimed aggregate versus dense graupel to represent the graupel category. By changing these particles, the tests also assess the impact of increasing the IWC on the reflectivities because these particles have an implied mass-dimensional relationship. The simulated reflectivities were highly sensitive to the riming assumptions on the aggregate category. In the stratiform shield case, both graupel tests could be used to simulate the HIWRAP reflectivity and DFR distributions by altering the riming on the aggregate particles. In contrast, in the anvil outflow, the graupel test using a dense graupel particle would overestimate compared to the HIWRAP reflectivities. The DFR results in this study focused on the Ku- and Ka-band because the MC3E aircraft observations from HIWRAP include only the Ku- and Ka-band. The DFR signal stands out for larger particles, and the difference in frequencies cannot be used to constrain microphysics of smaller particles. By expanding to include differences from additional frequencies (e.g. W, G), future work may analyze particle sizes and habits that are too small to influence the Ku-Ka.

In relating ice microphysics and radar remote sensing variables, there are numerous possible combinations and relationships. Some examples include mass-dimensional relationships, fallspeed relationships, and reflectivity and ice water content relationships. This study emphasizes that there are a range of outcomes that can produce the aircraft radar observations. It is important to assess the environmental and microphysical characteristics associated with these events for developing and constraining future radar retrievals and algorithms. By testing combinations of particles, we seek to develop an understanding of the hydrometeors simulated in a weather model and how those can be related to hydrometeors observed by a spaceborne radar. Upcoming satellite missions such as INCUS will observe deep convection and obtain convective mass flux; in-situ and remote sensing observations of ice particles in convective environments provide insights to the ice particles lofted upward. Future work should continue to expand upon analysis in a broader range of field campaigns with measurements in maritime, mountainous and other unique environments as INCUS will sample vast tropical and mid-latitude regions.

Acknowledgments. We thank the INCUS team broadly for their feedback and discussions on the MC3E results. This work was supported by NASA grants 80NSSC23M0083 (GMM), 80NSSC23M0011 (JAF), and through funding from NSF to NCAR (AJH). The work of JAS, MDL, and DJP was performed at the Jet Propulsion Laboratory, California Institute of Technology, under a contract with the National Aeronautics and Space Administration.

Data availability statement. MC3E Citation observations are available at https://ghrc.nsstc.nasa.gov/pub/fieldCampaigns/gpmValidation/mc3e/. MC3E HIWRAP observations were obtained from https://har.gsfc.nasa.gov/index.php?section=51 The University of Illinois/Oklahoma Optical Array Probe (OAP) Processing Software (UIOOPS v3.4; McFarquhar et al., 2018) was used to process the 2DC and HVPS data. The ARTS (doi:10.5281/zenodo.3727673) and snowScatt (10.5281/zenodo.3746261) databases are available online. NEXRAD observations were accessed from https://ghrc.nsstc.nasa.gov/pub/doc/gpmgv/mc3e/gpmnexradmc3e/gpmnexradmc3e_dataset.html#6. GOES13 observations were accessed online (Knapp, K. R. and S. Wilkins, 2017; doi:10.5194/essd-10-1417-2018).

References

Bouniol, D., J. Delanoë, C. Duroure, A. Protat, V. Giraud, and G. Penide, 2010: Microphysical characterisation of west african mcs anvils. *Quarterly Journal of the Royal Meteorological Society*, **136 (S1)**, 323–344.

Brown, P. R., and P. N. Francis, 1995: Improved measurements of the ice water content in cirrus using a total-water probe. *Journal of Atmospheric and Oceanic Technology*, **12 (2)**, 410–414.

Buehler, S. A., J. Mendrok, P. Eriksson, A. Perrin, R. Larsson, and O. Lemke, 2018: Arts, the atmospheric radiative transfer simulator–version 2.2. *Geoscientific Model Development*, **11 (4)**, 1537–1556.

Chase, R. J., S. W. Nesbitt, and G. M. McFarquhar, 2021: A dual-frequency radar retrieval of two parameters of the snowfall particle size distribution using a neural network. *Journal of Applied Meteorology and Climatology*, **60 (3)**, 341–359.

Chase, R. J., and Coauthors, 2018: Evaluation of triple-frequency radar retrieval of snowfall properties using coincident airborne in situ observations during olympex. *Geophysical Research Letters*, **45 (11)**, 5752–5760.

DeLaFrance, A., L. A. McMurdie, A. K. Rowe, and R. Conrick, 2024: Effects of riming on ice-phase precipitation growth and transport over an orographic barrier. *Journal of Advances in Modeling Earth Systems*, **16 (1)**, e2023MS003 778.

Delanoë, J., and R. J. Hogan, 2008: A variational scheme for retrieving ice cloud properties from combined radar, lidar, and infrared radiometer. *Journal of Geophysical Research: Atmospheres*, **113 (D7)**.

Dolan, B., B. Fuchs, S. Rutledge, E. Barnes, and E. Thompson, 2018: Primary modes of global drop size distributions. *Journal of the Atmospheric Sciences*, **75 (5)**, 1453–1476.

Dolan, B., S. A. Rutledge, and K. L. Rasmussen, 2022: Multiscale interactions contributing to enhanced orographic precipitation in landfalling frontal systems over the olympic peninsula. *Monthly Weather Review*, **150 (6)**, 1207–1231.

Dolan, B., and Coauthors, 2023: Time resolved reflectivity measurements of convective clouds. *Geophysical Research Letters*, **50 (22)**, e2023GL105 723.

Duffy, G., G. Mcfarquhar, S. W. Nesbitt, and R. Bennartz, 2021: Demonstration of a consistent relationship between dual-frequency reflectivity and the mass-weighted mean diameter in measurements of frozen precipitation from gcpex, olympex, and mc3e. *Journal of the Atmospheric Sciences*, **78 (8)**, 2533–2547.

Duffy, G., and D. J. Posselt, 2022: A gamma parameterization for precipitating particle size distributions containing snowflake aggregates drawn from five field experiments. *Journal of Applied Meteorology and Climatology*, **61 (8)**, 1077–1085.

Dzambo, A. M., G. McFarquhar, and J. A. Finlon, 2023: Quantifying uncertainty in ice particle velocity–dimension relationships using mc3e observations. *Journal of the Atmospheric Sciences*, **80 (1)**, 189–209.

Eriksson, P., R. Ekelund, J. Mendrok, M. Brath, O. Lemke, and S. A. Buehler, 2018: A general database of hydrometeor single scattering properties at microwave and sub-millimetre wavelengths. *Earth System Science Data*, **10 (3)**, 1301–1326.

Field, P., and A. Heymsfield, 2015: Importance of snow to global precipitation. *Geophysical Research Letters*, **42 (21)**, 9512–9520.

Finlon, J. A., G. M. McFarquhar, S. W. Nesbitt, R. M. Rauber, H. Morrison, W. Wu, and P. Zhang, 2019: A novel approach for characterizing the variability in mass–dimension relationships: Results from mc3e. *Atmospheric Chemistry and Physics*, **19 (6)**, 3621–3643.

Finlon, J. A., L. A. McMurdie, and R. J. Chase, 2022: Investigation of microphysical properties within regions of enhanced dual-frequency ratio during the impacts field campaign. *Journal of the Atmospheric Sciences*, **79 (10)**, 2773–2795.

Helmus, J. J., and S. M. Collis, 2016: The python arm radar toolkit (py-art), a library for working with weather radar data in the python programming language. *Journal of Open Research Software*, **4**.

Heymsfield, A., A. Bansemer, G. Heymsfield, D. Noone, M. Grecu, and D. Toohey, 2023: Relationship of multiwavelength radar measurements to ice microphysics from the impacts field program. *Journal of Applied Meteorology and Climatology*, **62 (3)**, 289–315.

Heymsfield, A. J., A. Bansemer, C. Schmitt, C. Twohy, and M. R. Poellot, 2004: Effective ice particle densities derived from aircraft data. *Journal of the atmospheric sciences*, **61 (9)**, 982–1003.

Heymsfield, A. J., C. Schmitt, and A. Bansemer, 2013a: Ice cloud particle size distributions and pressure-dependent terminal velocities from in situ observations at temperatures from 0 to- 86 c. *Journal of the Atmospheric Sciences*, **70 (12)**, 4123–4154.

Heymsfield, A. J., C. Schmitt, A. Bansemer, and C. H. Twohy, 2010: Improved representation of ice particle masses based on observations in natural clouds. *Journal of the Atmospheric Sciences*, **67 (10)**, 3303–3318.

Heymsfield, G. M., L. Tian, L. Li, M. McLinden, and J. I. Cervantes, 2013b: Airborne radar observations of severe hailstorms: Implications for future spaceborne radar. *Journal of applied meteorology and climatology*, **52 (8)**, 1851–1867.

Hogan, R. J., and C. D. Westbrook, 2014: Equation for the microwave backscatter cross section of aggregate snowflakes using the self-similar rayleigh–gans approximation. *Journal of the Atmospheric Sciences*, **71 (9)**, 3292–3301.

Holroyd III, E. W., 1987: Some techniques and uses of 2d-c habit classification software for snow particles. *Journal of Atmospheric and Oceanic Technology*, **4 (3)**, 498–511.

Hueholt, D. M., S. E. Yuter, and M. A. Miller, 2022: Revisiting diagrams of ice growth environments. *Bulletin of the American Meteorological Society*, **103 (11)**, E2584–E2603.

Hutson, A., C. Pettersen, A. Fujisaki-Manome, G. E. Mann, S. W. Nesbitt, and M. S. Kulie, 2025: Evaluating the performance of microphysics schemes against observations during high-impact lake-effect snow events. *Weather and Forecasting*.

Janisková, M., and M. D. Fielding, 2020: Direct 4d-var assimilation of space-borne cloud radar and lidar observations. part ii: Impact on analysis and subsequent forecast. *Quarterly Journal of the Royal Meteorological Society*, **146 (733)**, 3900–3916.

Jensen, M. P., and Coauthors, 2016: The midlatitude continental convective clouds experiment (mc3e). *Bulletin of the American Meteorological Society*, **97 (9)**, 1667–1686.

Kay, J., and Coauthors, 2012: Exposing global cloud biases in the community atmosphere model (cam) using satellite observations and their corresponding instrument simulators. *Journal of Climate*, **25 (15)**, 5190–5207.

King, F., C. Pettersen, B. Dolan, J. Shates, and D. Posselt, 2024: Primary modes of northern hemisphere snowfall particle size distributions. *Journal of the Atmospheric Sciences*, **81 (12)**, 2093–2113.

Knapp, K. R., and S. L. Wilkins, 2018: Gridded satellite (gridsat) goes and conus data. *Earth System Science Data*, **10 (3)**, 1417–1425.

Kneifel, S., M. Kulie, and R. Bennartz, 2011: A triple-frequency approach to retrieve microphysical snowfall parameters. *Journal of Geophysical Research: Atmospheres*, **116 (D11)**.

Kollias, P., B. Puidgomènech Treserras, A. Battaglia, P. C. Borque, and A. Tatarevic, 2023: Processing reflectivity and doppler velocity from earthcare's cloud-profiling radar: the c-fmr, c-cd and c-apc products. *Atmospheric Measurement Techniques*, **16 (7)**, 1901–1914.

Korolev, A., J. Strapp, G. Isaac, and E. Emery, 2013: Improved airborne hot-wire measurements of ice water content in clouds. *Journal of Atmospheric and Oceanic Technology*, **30 (9)**, 2121–2131.

Krämer, M., and Coauthors, 2020: A microphysics guide to cirrus–part 2: Climatologies of clouds and humidity from observations. *Atmospheric Chemistry and Physics*, **20 (21)**, 12 569–12 608.

Kumjian, M. R., S. Mishra, S. E. Giangrande, T. Toto, A. V. Ryzhkov, and A. Bansemer, 2016: Polarimetric radar and aircraft observations of saggy bright bands during mc3e. *Journal of Geophysical Research: Atmospheres*, **121 (7)**, 3584–3607.

Lawson, R., and Coauthors, 2019: A review of ice particle shapes in cirrus formed in situ and in anvils. *Journal of Geophysical Research: Atmospheres*, **124 (17-18)**, 10 049–10 090.

Leinonen, J., and W. Szyrmer, 2015: Radar signatures of snowflake riming: A modeling study. *Earth and Space Science*, **2 (8)**, 346–358.

Li, D., C. Zhao, Z. Yue, C. Liu, Y. Sun, and J. B. Cohen, 2022: Response of cloud and precipitation properties to seeding at a supercooled cloud-top layer. *Earth and Space Science*, **9 (9)**, e2021EA001 791.

Li, D., and Coauthors, 2024: Seeding invigoration effect of ice-containing clouds on lower convective clouds during meiyu season in 2020. *Atmospheric Research*, **301**, 107 288.

Li, L., and Coauthors, 2015: The nasa high-altitude imaging wind and rain airborne profiler. *IEEE Transactions on Geoscience and Remote Sensing*, **54 (1)**, 298–310.

Libbrecht, K. G., 2017: Physical dynamics of ice crystal growth. *Annual Review of Materials Research*, **47 (1)**, 271–295.

Liu, C.-L., and A. J. Illingworth, 2000: Toward more accurate retrievals of ice water content from radar measurements of clouds. *Journal of applied meteorology*, **39 (7)**, 1130–1146.

Liu, S., C. Zhao, Y. Zhou, Z. Wu, and Z. Hu, 2022: Multi-case analysis of ice particle properties of stratiform clouds using in situ aircraft observations in hebei, china. *Atmosphere*, **13 (2)**, 200.

Locatelli, J. D., and P. V. Hobbs, 1974: Fall speeds and masses of solid precipitation particles. *Journal of Geophysical Research*, **79 (15)**, 2185–2197.

Maahn, M., U. Löhnert, P. Kollias, R. C. Jackson, and G. M. McFarquhar, 2015: Developing and evaluating ice cloud parameterizations for forward modeling of radar moments using in situ aircraft observations. *Journal of Atmospheric and Oceanic Technology*, **32 (5)**, 880–903.

Maahn, M., D. D. Turner, U. Löhnert, D. J. Posselt, K. Ebell, G. G. Mace, and J. M. Comstock, 2020: Optimal estimation retrievals and their uncertainties: What every atmospheric scientist should know. *Bulletin of the American Meteorological Society*, **101 (9)**, E1512–E1523.

Mace, G. G., A. Protat, S. Benson, and P. McGlynn, 2023: Inferring the properties of snow in southern ocean shallow convection and frontal systems using dual-polarization c-band radar. *Journal of Applied Meteorology and Climatology*, **62 (4)**, 467–487.

Maherndl, N., M. Maahn, F. Tridon, J. Leinonen, D. Ori, and S. Kneifel, 2023: A riming-dependent parameterization of scattering by snowflakes using the self-similar rayleigh–gans approximation. *Quarterly Journal of the Royal Meteorological Society*, **149 (757)**, 3562–3581.

Marinescu, P., S. van den Heever, S. Saleeby, and S. Kreidenweis, 2016: The microphysical contributions to and evolution of latent heating profiles in two mc3e mcss. *Journal of Geophysical Research: Atmospheres*, **121 (13)**, 7913–7935.

Mascio, J., Z. Xu, and G. G. Mace, 2017: The mass-dimensional properties of cirrus clouds during tc4. *Journal of Geophysical Research: Atmospheres*, **122 (19)**, 10–402.

Matrosov, S. Y., M. Maahn, and G. De Boer, 2019: Observational and modeling study of ice hydrometeor radar dual-wavelength ratios. *Journal of Applied Meteorology and Climatology*, **58 (9)**, 2005–2017.

McFarquhar, G. M., J. A. Finlon, D. M. Stechman, W. Wu, R. Jackson, and M. Freer, 2018: University of illinois/oklahoma optical array probe (oap) processing software.

McMurdie, L. A., and Coauthors, 2022: Chasing snowstorms: The investigation of microphysics and precipitation for atlantic coast-threatening snowstorms (impacts) campaign. *Bulletin of the American Meteorological Society*, **103 (5)**, E1243–E1269.

Nakaya, U., 1954: *Snow crystals: natural and artificial*. Harvard University Press.

Ori, D., L. von Terzi, M. Karrer, and S. Kneifel, 2021: snowscatt 1.0: consistent model of microphysical and scattering properties of rimed and unrimed snowflakes based on the self-similar rayleigh–gans approximation. *Geoscientific Model Development*, **14 (3)**, 1511–1531.

Oue, M., A. Tatarevic, P. Kollias, D. Wang, K. Yu, and A. M. Vogelmann, 2020: The cloud-resolving model radar simulator (cr-sim) version 3.3: description and applications of a virtual observatory. *Geoscientific Model Development*, **13 (4)**, 1975–1998.

Prein, A. F., and A. J. Heymsfield, 2020: Increased melting level height impacts surface precipitation phase and intensity. *Nature Climate Change*, **10 (8)**, 771–776.

Roh, W., M. Satoh, Y. Hagihara, H. Horie, Y. Ohno, and T. Kubuta, 2023: An evaluation of microphysics in a numerical model using doppler velocity measured by ground-based radar for application to the earthcare satellite. *EGUsphere*, **2023**, 1–20.

Schima, J., and Coauthors, 2024: A multi-probe automated classification of ice crystal habits during the impacts campaign. *Journal of Geophysical Research: Atmospheres*, **129 (22)**, e2024JD040 895.

Schumacher, C., and A. Funk, 2023: Assessing convective-stratiform precipitation regimes in the tropics and extratropics with the gpm satellite radar. *Geophysical Research Letters*, **50 (14)**, e2023GL102 786.

Stechman, D. M., G. M. McFarquhar, R. M. Rauber, B. F. Jewett, and R. A. Black, 2020: Composite in situ microphysical analysis of all spiral vertical profiles executed within bamex and pecan mesoscale convective systems. *Journal of the atmospheric sciences*, **77 (7)**, 2541–2565.

Stephens, G. L., K. A. Shiro, M. Z. Hakuba, H. Takahashi, J. A. Pilewskie, T. Andrews, C. J. Stubenrauch, and L. Wu, 2024: Tropical deep convection, cloud feedbacks and climate sensitivity. *Surveys in Geophysics*, 1–29.

Sy, O. O., and Coauthors, 2020: Impact of mass–size parameterizations of frozen hydrometeors on microphysical retrievals: Evaluation by matching radar to in situ observations from gcpex and olympex. *Journal of Atmospheric and Oceanic Technology*, **37 (6)**, 993–1012.

Tanelli, S., S. L. Durden, and E. Im, 2006: Simultaneous measurements of ku-and ka-band sea surface cross sections by an airborne radar. *IEEE Geoscience and remote sensing letters*, **3 (3)**, 359–363.

Tridon, F., and Coauthors, 2019: The microphysics of stratiform precipitation during olympex: Compatibility between triple-frequency radar and airborne in situ observations. *Journal of Geophysical Research: Atmospheres*, **124 (15)**, 8764–8792.

van den Heever, S., 2021: Nasa selects new mission to study storms, impacts on climate models. *NASA Earth*.

Wang, J., X. Dong, and B. Xi, 2015: Investigation of ice cloud microphysical properties of dcss using aircraft in situ measurements during mc3e over the arm sgp site. *Journal of Geophysical Research: Atmospheres*, **120 (8)**, 3533–3552.